Provided for non-commercial research and education use.
Not for reproduction, distribution or commercial use.

This article appeared in a journal published by Elsevier. The attached copy is furnished to the author for internal non-commercial research and education use, including for instruction at the authors institution and sharing with colleagues.

Other uses, including reproduction and distribution, or selling or licensing copies, or posting to personal, institutional or third party websites are prohibited.

In most cases authors are permitted to post their version of the article (e.g. in Word or Tex form) to their personal website or institutional repository. Authors requiring further information regarding Elsevier's archiving and manuscript policies are encouraged to visit:

http://www.elsevier.com/copyright

Author's personal copy

Continental Shelf Research 30 (2010) 1963–1970

Contents lists available at ScienceDirect

Continental Shelf Research

journal homepage: www.elsevier.com/locate/csr

Research papers

Variation of overtides by wave enhanced bottom drag in a North Florida tidal inlet

I. Safak *, A. Sheremet, A. Valle-Levinson, A.F. Waterhouse

Department of Civil and Coastal Engineering, University of Florida, 365 Weil Hall, P.O. Box 116590, Gainesville, FL 32611, USA

ARTICLE INFO

Article history:
Received 2 February 2010
Received in revised form
10 September 2010
Accepted 15 September 2010
Available online 21 September 2010

Keywords:
Shallow water tides
Water waves
Drag coefficient
Bottom friction
Tidal inlets

ABSTRACT

Month-long observations of waves and tidal currents at Ponce de Leon Inlet, North Florida are used to investigate the importance of wave-induced bottom drag as a mechanism for overtide generation in estuaries. While bottom drag can in theory lead to overtide generation, in practice, resolving unambiguously this effect is difficult as it tends to be overshadowed by the stronger effect of diurnal–semidiurnal tidal variance. Bottom boundary layer numerical simulations based on observational data suggest that waves can cause the bottom drag experienced by currents to increase by a factor of 1.7, compared with relatively calm conditions. Despite the relatively short duration and limited scope of the experiment, the analysis suggests that overtide modulations (East–West velocity components of the 5th and 6th diurnal constituents) are correlated with wave-enhanced drag trends. Therefore, wave-enhanced bottom drags may be enhancing generation of overtides. Further work is necessary to understand the scope and the strength of this mechanism, in relation to the characteristics (e.g., flow direction) of individual overtides.

© 2010 Elsevier Ltd. All rights reserved.

1. Introduction

Surface gravity waves are known to affect the circulation in shallow estuaries by slowing down the flow (Signell et al., 1990), and modifying the near-bed Reynolds stresses (Bricker et al., 2005). In general, bottom boundary layer processes associated with surface waves, such as near-bed turbulence (e.g., Grant and Madsen, 1979, 1986), generation of sand ripples (e.g., Nielsen, 1992), and near-bed sheet flows (e.g., Styles and Glenn, 2000), increase the bottom drag experienced by currents in coastal shallow waters and estuaries. On a larger temporal scale, tidal distortions (overtides associated with tidal asymmetries) play an important role in the long-term inlet and channel morphodynamics in estuaries (Friedrichs and Aubrey, 1994) and can induce tidal-residual flow in coastal lagoons. The relation between bottom drag variability and overtide generation has been hypothesized (Parker, 1991) and demonstrated (e.g., Dworak and Gomez-Valdes, 2005), but the possible connection between wave-induced bottom drag and overtide generation has not been investigated in depth.

Overtide generation is associated with the nonlinearities of the governing equations. In a flat-bottom, straight tidal channel of constant width and constant depth h, the evolution of the surface elevation η and along-channel, vertically integrated velocity u is governed by the shallow-water equations for mass and momentum conservation

$$\frac{\partial \eta}{\partial t}+h\frac{\partial u}{\partial x}=-\frac{\partial}{\partial x}\eta u, \tag{1}$$

$$\frac{\partial u}{\partial t}+g\frac{\partial \eta}{\partial x}=-u\frac{\partial u}{\partial x}-C_d\frac{u|u|}{h+\eta}, \tag{2}$$

where t is the time, x is the along-channel distance, g is the gravitational acceleration, and C_d is the bottom drag coefficient. The effects of Earth's rotation and horizontal turbulence are neglected. The nonlinear terms on the right-hand side of these equations (nonlinear continuity term in Eq. (1), advective term and quadratic bottom friction term in Eq. (2)) are responsible for the generation of harmonics of the fundamental tidal signal (overtides), and a zero-frequency residual (Parker, 2007). Substituting into Eqs. (1) and (2) the Fourier series

$$\begin{pmatrix}\eta(t)\\ u(t)\end{pmatrix}=\sum_{n=-\infty}^{\infty}\begin{pmatrix}A_n(\varepsilon t)\\ U_n(\varepsilon t)\end{pmatrix}\exp(i\omega_n t), \tag{3}$$

with $\omega_{-n}=\omega_n$, $A_{-n}=A_n^*$, $U_{-n}=U_n^*$ (asterisk denotes complex conjugation) and εt a slow time dependence (ε being a small parameter of the problem, e.g., tidal amplitude over depth), transforms the nonlinear terms to the generic form

$$\partial_t U_n \sim \sum_{p,q=-\infty}^{\infty} T_{j,p,q}U_pU_q\delta_{p+q,n}, \tag{4}$$

* Corresponding author. Tel.: +1 352 392 95 37x1410.
E-mail addresses: ilgar@ufl.edu (I. Safak), alex@coastal.ufl.edu (A. Sheremet), arnoldo@ufl.edu (A. Valle-Levinson), awaterhouse@ufl.edu (A.F. Waterhouse).

0278-4343/$ - see front matter © 2010 Elsevier Ltd. All rights reserved.
doi:10.1016/j.csr.2010.09.007

Author's personal copy

where δ is the Kronecker symbol, and $T_{j,p,q}$ is an interaction coefficient depending in general on the frequency of the interacting components. One of the effects of the nonlinear terms is the transfer of variance between the different spectral modes. If indices p and q are positive, their interaction contributes to the harmonic $n=p+q$. For example, sum interaction of the semidiurnal tide M_2 with itself, i.e., $\omega_p=\omega_q=2\pi/(12.42\,\text{h})$, generates the fourth-diurnal tide M_4 with $\omega_n=\omega_p+\omega_q=2\pi/(6.21\,\text{h})$; sum interaction of M_2 with M_4, i.e., $\omega_p=2\pi/(12.42\,\text{h})$ and $\omega_q=2\pi/(6.21\,\text{h})$, generates the sixth-diurnal tide M_6 with $\omega_n=\omega_p+\omega_q=2\pi/(4.14\,\text{h})$, etc. Thus, a harmonic "exists" in Eqs. (1) and (2) independent of whether it has detectable variance, and independent of the mechanism that generates it. Following the conceptual model (Eq. (4)), the term "harmonic" will be used in this study together with the term "overtides" to denote a sum of two frequencies (e.g., integer multiples of the diurnal frequency) in the Fourier representation.

The conceptual model (Eq. (4)) shows that the efficiency of nonlinear spectral transfers depends on the variance of the forcing p–q modes (right-hand side of Eq. (4)), and the magnitude of the interaction coefficient $T_{j,p,q}$. Because the variability of $T_{j,p,q}$ is weak, the interaction coefficients are typically assumed constant. However, this is not necessarily the case for the bottom drag coefficient C_d in Eq. (2), as bottom drag can vary because of external influences (e.g., bottom sediment, vegetation, internal turbulence). The nonlinear term in Eq. (4) scales linearly with the drag coefficient, and is quadratic in amplitudes. This implies that drag variability has an inherently weaker expression on overtide modulation than the variability of spectral density of variance. For example, in the dominant second harmonic generation (self-interaction $p=q$), a factor of 2 increase in the amplitude of mode p increases the nonlinear term by a factor of 4. Therefore, the overtide generation effect of waves through enhanced bottom drag could be detected in favorable conditions, e.g., characterized by low tidal variance and energetic wave-induced bottom turbulence. This mechanism is investigated herein, based on a 1-month data set collected in Ponce de Leon Inlet, Florida by using a bottom boundary layer model and applying tidal analysis.

2. Field experiment

Currents and waves were measured between December 14th, 2007 and January 14th, 2008, in Ponce de Leon Inlet in the Atlantic Coast of Florida, USA using a 1228.8 kHz Acoustic Doppler Current Profiler (ADCP, Teledyne RD Instruments). The ADCP was deployed at the lagoon to the south of the inlet mouth, pointing upward, in about 3-m water depth (Fig. 1a). The built-in pressure sensor of the instrument was located at 0.40 m above the bottom (mab). The ADCP sampled velocity in 50-cm bins, with the lowest bin centered at 1.05-m distance from the transducer. Valid measurements were therefore recorded only at the two lowest measurement bins (centered at 1.45 and 1.95 mab, respectively). The 1.45-mab bin was below the water surface during the entire duration of the experiment; part of the 1.95-mab bin was above the water surface during January 12–13, 2008. Both measurement points were well outside of the wave boundary layer, which is a few cm thick and therefore much thinner than the current boundary layer which scales with water depth (e.g., Fredsoe and Deigaard, 1992). Because the numerical model used here (Styles and Glenn, 2000, see Section 3) requires a single current measurement point, our discussion will focus on the 1.45-mab (lowest bin) observations.

The ADCP sampled flow velocity at 1.5-s pings, and recorded 10-min averages (400 velocity samples). One-hour averages of the velocity observations were transformed to North-South (positive northward) and East–West (positive eastward) coordinate frame. Wave observations combined 17-min/h measurements of pressure, acoustic surface track and velocity profiles (sampled at 2-Hz, 2048 samples per burst) to estimate the wave directional spectrum at frequency resolution of $\Delta f=0.0078$ Hz and angular resolution of $\Delta\theta=4^\circ$. The measured spectra were converted to the spectral estimates at the surface by applying a linear transfer function (e.g., Dean and Dalrymple, 1991). For this, the wave-number k was calculated through the linear dispersion relationship which accounts for the effect of tidal current on waves (Kirby and Chen, 1989; Smith, 2002):

$$2\pi f = kU\cos(\xi-\alpha)+\sqrt{gk\tanh(kh)}, \tag{5}$$

where U is the current speed, ξ is the current direction, and α is the wave direction. Due to wave attenuation with depth, observations of bottom pressure cannot resolve high-frequency spectral bands. Here, frequency bands with variance at sensor $<2\%$ of surface variance were assumed to follow the f^{-5} spectral tail law (Phillips, 1958). Directional spectra produced by the wave processing packages WavesMon and WaveView (Teledyne RD Instruments) were cross-checked against pressure data by

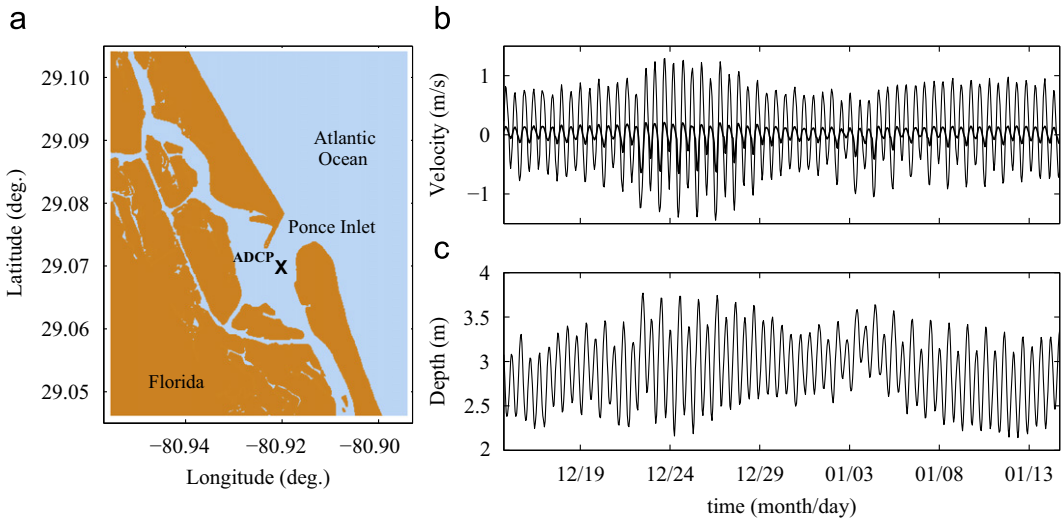

Fig. 1. Experiment site, and time evolution of the tidal observations. (a) Top view of Ponce de Leon Inlet, Florida. The "x" indicates the location of the ADCP. (b) One-hour averages of North–South (thin line, positive northward) and East–West (thick line, positive eastward) components of current velocity. (c) Mean water depth at the measurement location.

Author's personal copy

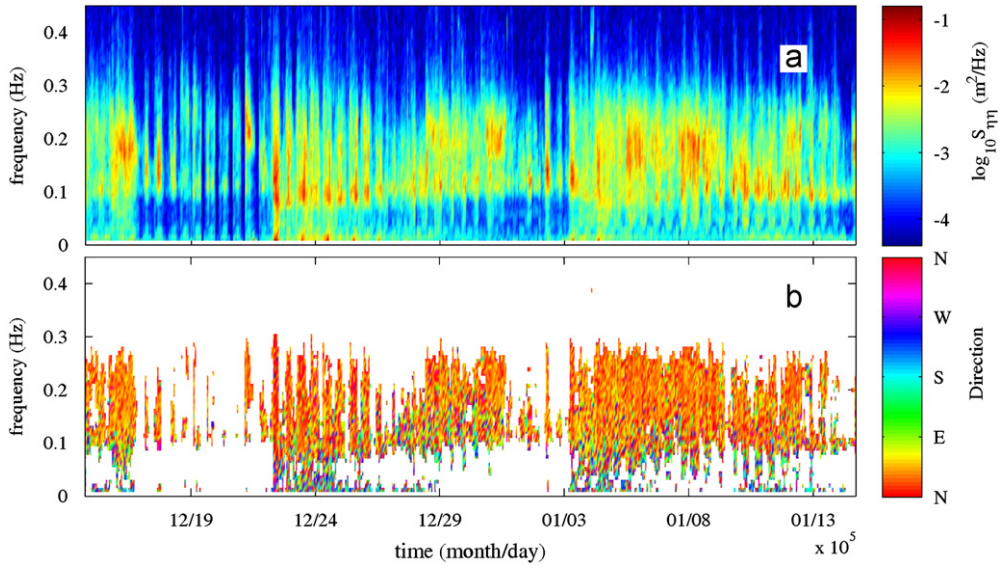

Fig. 2. (Color online) Time evolution of wave spectral estimates obtained from the ADCP data set. (a) Spectral density of sea surface elevation. (b) Peak wave propagation direction (N means from North) for each frequency band in the power spectrum (panel a). Directions are shown only for frequencies with spectral density $>10^{-3}\mathrm{m}^2/\mathrm{Hz}$.

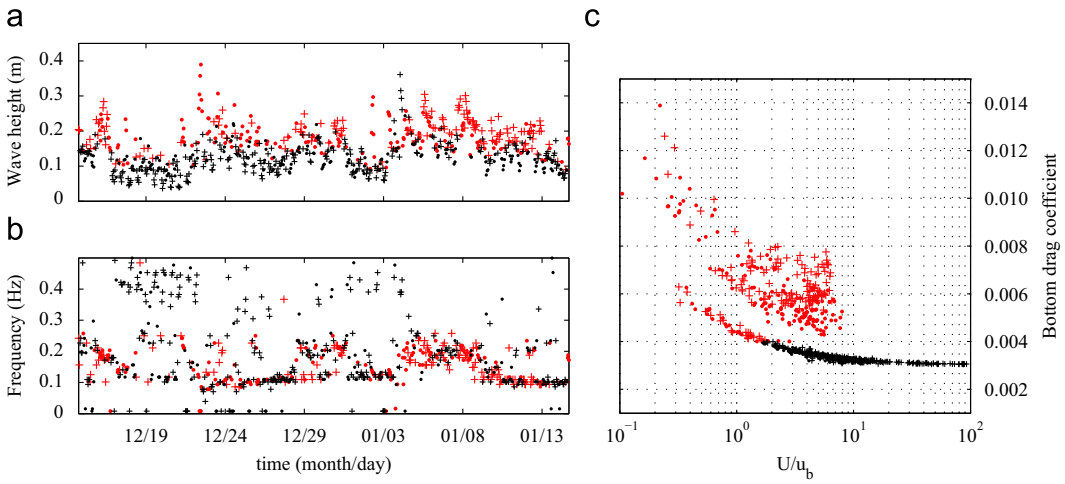

Fig. 3. Wave observations and bottom drag calculations. Time evolution of: (a) significant wave height; and (b) peak wave frequency. (c) Model estimates of the bottom drag coefficient C_d versus observations of ratio of mean current speed U to wave orbital velocity u_b. Black and grey symbols correspond to low and high drag events, respectively. Crosses and dots correspond to ebb and flood phases of the tide in the inlet, respectively.

comparing wave heights and peak frequencies. A summary of the observations is shown in Figs. 1–3. Due to the geography of the inlet at the location of the ADCP (Fig. 1a), the North–South velocity component was dominant (Fig. 1b). During ebb and flood, the main direction of the current was rotated approximately 10° clockwise from the North–South axis. A period of relatively higher current velocities (December 23–27th, 2007) was associated with spring tides (Figs. 1b and c), characterized by tidal ranges of ~1.6 m, resulting in water depth variations between 2.2 and 3.8 m. Remarkably, together with locally generated short waves (period of about 5 s), swell (7–10 s) was often present in the observations, and even infragravity waves (period >20 s) which suggests a combination of locally generated short waves and coastal ocean waves propagating through the inlet (Fig. 2a). Due to the geometry of the inlet, the dominant wave direction at the location of the sensor was approximately from the North-Northeast sector throughout the experiment (Fig. 2b). Wave height was strongly modulated by the tide level (e.g., Fig. 1c), with larger waves occurring during high tide. Wave height was typically between 15 and 20 cm (Fig. 3a), with a slightly more energetic and better organized wave-field observed during the second half of the experiment. Frequency peaks also indicate the presence of swell and locally generated short waves (Fig. 3b).

3. Results

3.1. Bottom stress and drag coefficient

The drag coefficient can be estimated from its relation with the bottom stress, $\tau_b=\rho u_*^2=\rho C_d U^2$, equivalent to $C_d=(u_*/U)^2$, where u_* is the bottom friction velocity, and ρ is the density of water. The lack of near-bed velocity observations (measurement points are 1.45 mab and above) precludes direct estimation of wave-induced bottom stress from data, for example by fitting a logarithmic profile to the vertical profile of the current (e.g., Lueck and Lu,

Author's personal copy

1997). Methods developed for estimating Reynolds stress are generally based on the use of cross-correlation of horizontal and vertical velocity fluctuations. Methods which use ADCP along-beam velocities but do not account for wave-bias (e.g., Lohrmann et al., 1990; Stacey et al., 1999) can severely overestimate Reynolds stresses in a wave-dominated environment. Eliminating wave-bias from Reynolds stress estimates usually requires either strong additional assumptions – when using a single point measurement (e.g., Bricker and Monismith, 2007) – or an elaborate experimental setup with multiple measurement points carefully chosen (e.g., Shaw and Trowbridge, 2001; Rosman et al., 2008). In addition, any of these methods can only provide estimates of the stress at the measurement location. Further assumptions (models), e.g., about bottom roughness values, are often needed to relate these Reynolds stress estimates to the bottom stress τ_b.

Current measurements from a single point in the water column (located at 1.45 mab) can be considered misleading to get results related to wave-induced friction. Therefore, a numerical model which requires current measurements only at a single point in the water column to account for wave–current interaction on the bottom boundary layers above sandy beds is used (Styles and Glenn, 2000). In this model, turbulence closure is achieved by a time-invariant eddy viscosity profile, and bottom friction velocity u_* is estimated as a function of bottom roughness, waves and suspended sediment-induced stratification. In the model formulation, three factors contribute to the bottom roughness: the individual sediment grains; wave-generated ripples (bedforms of height η_r and length λ_r); and a near-bed transport layer, which is formed when the ripples are washed out during stronger flows. The model does not require instantaneous fluctuations, instead, the demeaned part of the time-series of flow field is represented by mean wave parameters. The model uses the mean flow velocity U at a given height z_r above the bed, the bottom wave orbital velocity and excursion amplitude (u_b and A_b), the angle between mean current and wave direction, and grain-size of the bottom sediment. The model was run assuming that the ADCP velocity measurements at z_r=1.45 mab represent the free-flow velocity. The amplitudes u_b and A_b were estimated for each measurement burst as

$$u_b = \frac{H_s \pi f_p}{\sinh(k_p h)}, \quad A_b = \frac{u_b}{2\pi f_p}, \tag{6}$$

using the linear wave approximation for a monochromatic wave of significant wave height H_s with frequency f_p (equal to the spectral peak frequency) and wavenumber k_p satisfying the linear dispersion relationship (Eq. (5)). The spectral peak direction was taken as the representative direction of waves for each burst. The bed material for Ponce de Leon Inlet was assumed to be quartz sand with a specific gravity of $s=\rho_{sand}/\rho=2.65$, and a median grain-size of d=0.21 mm (Hughes, 1999). The following empirical relationship is given by Styles and Glenn (2002) to determine the ripple height η_r:

$$\frac{\eta_r}{A_b} = \begin{cases} 0.30X^{-0.39}, & X \le 2, \\ 0.45X^{-0.99}, & X \ge 2. \end{cases} \tag{7}$$

X is a nondimensional parameter defined as $X=\theta_m/S_*$ where θ_m is the mobility number which is the ratio of the wave-induced disturbing force to the stabilising force due to gravity, and S_* is the nondimensional sediment parameter, respectively (Nielsen, 1992):

$$\theta_m = \frac{u_b^2}{(s-1)gd}, \quad S_* = \frac{d}{4\nu}\sqrt{(s-1)gd}, \tag{8}$$

where ν is the kinematic viscosity of water. Fig. 3c shows estimates of the bottom drag coefficient (C_d) based on the Styles and Glenn (2000) model. Numerical simulations that neglect wave effects yield $C_d = 3.0\times10^{-3}$. When wave effects are taken into account, observations separate into two groups (black and grey symbols in Fig. 3): one characterized by drag average $C_d = 3.2\times10^{-3}$ (black symbols); the other yielding an average value about 1.7 times larger, $C_d = 5.5\times10^{-3}$ (grey symbols). High drag values are associated with relatively higher wave heights (Fig. 3a) and lower peak frequencies (Fig. 3b). Large wave heights and low frequencies seem to be equally important: 90% of the measurement bursts associated with the increased bottom drag are characterized by waves with $H_s > 0.15$ m and $f_p < 0.25$ Hz. For high and low drag events, there is no clear separation depending on ebb (black and grey crosses in Fig. 3) and flood (black and grey dots in Fig. 3) phases of the tide in the inlet.

There was no instrumentation available to observe bedform evolution and the structure of the bottom boundary layer flow. Nonetheless, the effect of sand ripples and sheet flows on bottom drag is accounted for in these calculations with the default representation of these processes implemented in the model. For the wave–current conditions in the present data set, the model sand ripples are characterized by heights rarely exceeding 4 cm (Fig. 4a), and approximately constant steepness $\frac{1}{7}$ (ripple wave length between 10 and 35 cm).

Results of numerical tests of the role played by different drag mechanisms (wave-induced bottom turbulence, bedforms, sheet flows, and grain size) in generating bottom drag are shown in Fig. 4b. The bottom drag induced by bed granularity (sediment grains) is approximately $C_d=10^{-3}$. Over a smooth bed (no sand ripples) wave-induced turbulence increases slightly the drag, about 10% on average. The effect of sand ripples alone (other wave effects are neglected) results in a drag coefficient ranging between 3.2×10^{-3} and 4.5×10^{-3}. The lower value is close to the lower range of the full calculation of the bottom drag result (black crosses and dots in Figs. 3c and 4b). This lower range of the full calculations corresponds to cases when the wave-induced disturbing force is less than necessary to modify the bedforms with default height in the model $\eta_r = 1$ cm (black crosses and dots in Figs. 3 and 4). Cases with higher C_d occur in the presence of waves effective to generate ripples with greater height, which enhance the bottom drag (grey crosses and dots in Figs. 3 and 4). No significant variation is observed for ebb and flood conditions. Overall, the numerical tests suggest that the clear separation between high and low total drag calculations (Fig. 3c) is due to these wave-generated ripples (grey crosses and dots in Figs. 3 and 4).

3.2. Tide analysis

Fig. 5 shows the results of a harmonic analysis using the software package T_TIDE (Pawlowicz et al., 2002) based on mean currents, which includes (Rayleigh criterion 1.0) 29 tidal constituents: the fortnightly component, eight diurnals, four semidiurnals, and 16 components with frequencies higher than the semidiurnals. Only the significant constituents, with the squared ratio of amplitude to the error in amplitude greater than 1, are shown. This was satisfied by 11 and 17 constituents for North–South and East–West, respectively. For both components, the tidal components M_2, N_2 and K_1 dominate the signal, and the fourth diurnal constituent M_4 with a frequency of about 3.86 cycles per day (cpd) is the overtide with the highest amplitude.

Together with the T_TIDE amplitude spectrum, the Fourier amplitude spectrum (10 degrees of freedom) is also shown in Fig. 5. The regular Fourier analysis provides an estimate of the variance of tidal constituents over the entire duration of the experiment. Investigating the evolution of specific constituents

Author's personal copy

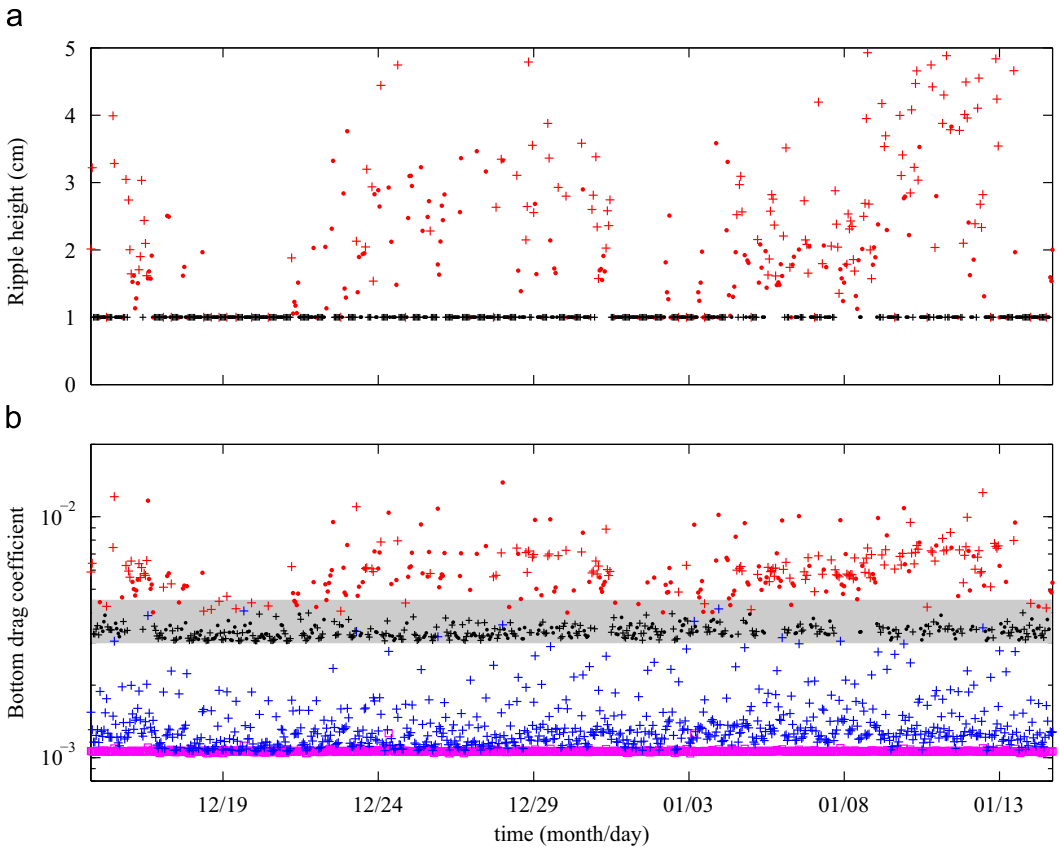

Fig. 4. Time evolution, calculated for the entire data set duration, of (a) ripple height, calculated by the Styles and Glenn (2000) model in full drag calculations (black and grey symbols correspond to low and high drag events, respectively, same as in Fig. 3). Ripple steepness is approximately constant at $\frac{1}{7}$, as given by Styles and Glenn (2002). (b) Estimates of the drag effect of various drag-generating mechanisms. Continuous line: bottom drag in the absence of waves, over a perfectly smooth bed (no bed ripples). Triangles: bottom drag over a perfectly smooth bed, with waves accounted for. Gray shaded area: the range of bottom drag induced by sand ripples, as represented by the model (ripple dimension varying between 1-cm height, 15-cm wave length—lower edge, and 3.5-cm height and 40-cm wave length—upper edge). Black and grey crosses and dots: full drag calculations.

require time–frequency analysis techniques such as the "complex demodulation" method (e.g., Dworak and Gomez-Valdes, 2005), or complete orthogonal decomposition approaches such as the Gabor or wavelet transforms (e.g., Carmona et al., 1998). The Gabor transform used here has the advantage that it is closely related to the traditional Fourier analysis and explains completely the variance of the signal. The decomposition is calculated with a sliding 100-h window (roughly 26 periods of the M_4 harmonic) and 98% overlap. The resulting time–frequency analysis yields a 51-point frequency grid (increment $\Delta f = 0.24$ cpd) and 323 time points with increment $\Delta t = 2$ h. To simplify the discussion of the results of this analysis, frequency bands will be referred to as "diurnal harmonics", based on the relation between their center frequency and the diurnal frequency. The term is meant to denote spectral modes with frequencies multiple of the diurnal frequency, with no reference to a particular generation mechanism. These bands contain, but should not be identified with, tidal constituents such as M_3, M_4, and others.

The main goal of this analysis is to identify trends that are common to overtide and wave-induced drag variability. As discussed in Section 1, the evolution of harmonic n (conceptual model equation (4)) is primarily governed by the variance at all lower frequencies (right-hand side modes p and q). For example, the 6th diurnal harmonic ($n=6f_0$, with f_0 frequency of the diurnal constituent) is modulated by the variance in all lower frequency bands (all modes p and q, such that $p+q=n$). However, the semidiurnal band dominates the spectrum by accounting for, on average, 92% and 81% of the total variance at the frequencies $f < 2.2$ cpd for North–South and East–West components of velocity, respectively (Fig. 5). Therefore, we will restrict our estimate of the forcing variance to the semidiurnal band.

The semidiurnal variability is expected to be too strong, most of the time, to allow for the detection of drag-variability effects on overtides. Even if the variance forcing is weak, and waves are high (bottom drag effect is strong), it will still be difficult to identify the drag effect if the evolution trends of the drag and variance components of the forcing are similar. Therefore, it is hypothesized that optimal conditions for the detection of overtide modulation by bottom drag are realized when the variance of the semidiurnal band is low, waves are energetic (wave-induced drag is high), and the trends of bottom drag and semidiurnal variance are distinct.

Visual inspection of the North–South velocity component of overtides does not suggest a significant correlation with the bottom drag and therefore, North–South velocity components are not discussed here. All East–West components of diurnal harmonics (Figs. 6a–d) correlate with the semidiurnal variance (Fig. 6f) in the first half of the experiment. In particular, the frequency bands corresponding to the 3rd and 4th diurnal harmonics (bands that include the M_3 and M_4 constituents; Figs. 6a and b) follow the variance trends throughout the experiment, including the spring tide peak on December 24th (Fig. 6f, labelled "Variance"), as well as the smaller pulse starting on January 3rd. The fact that the initial increase observed in the drag coefficient (starting on December 19th; Fig. 6e) coincides with the beginning of the first spring tide during this month

Author's personal copy

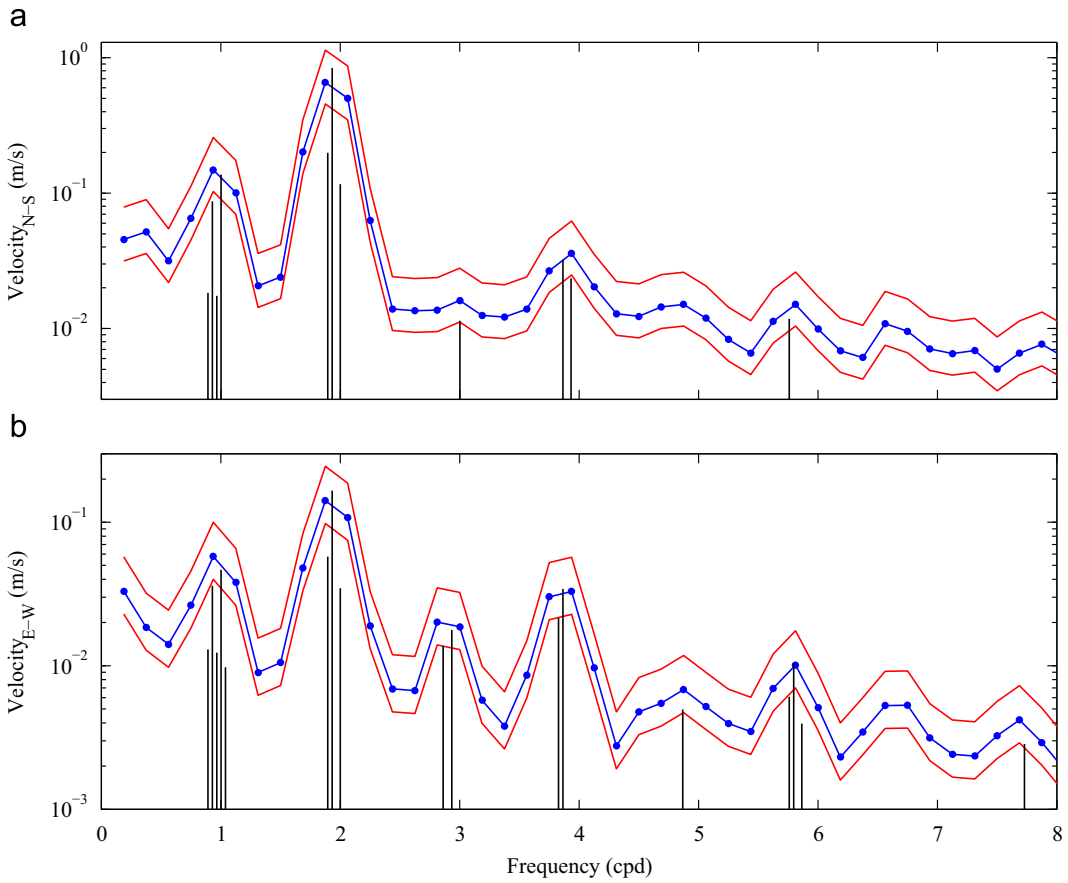

Fig. 5. Results of the tidal analysis: amplitude spectra of (a) North–South; and (b) East–West components of the flow velocity (dotted line: Fourier spectrum; bars: analysis based on T_TIDE (Pawlowicz et al., 2002)). Dashed lines mark 95% confidence limits for Fourier spectrum (Jenkins and Watts, 1968). The scaling for ordinates is different in (a) and (b).

reduces the chances of detecting the drag effects in the first half of the experiment period. However, during the second half of the experiment (January 1st to January 13th, labelled "Bottom drag" in Fig. 6), conditions became favorable for observing a possible contribution of the drag effects: tidal current amplitudes were smaller during that period due to the apogee–perigee effect, while the bottom drag increased by about 12% compared to the first half of the experiment (labelled "Variance"). During this period, the 5th and 6th diurnal harmonics have trends different than the 3rd and the 4th diurnal harmonics in the sense that they do not follow the pulse of increasing variance starting on January 3rd. Especially, the 5th diurnal harmonic does appear to follow the increasing drag trend (Fig. 6).

The correlations between overtide amplitudes and semidiurnal variance, and the correlations between overtide amplitudes and wave-induced drag are calculated with running windows of size varying between 100 and 300 h. The correlations show the same trend, however, those that are calculated with a 100-h window are rather noisy. The 150- and 200-h windows show a smooth and consistent evolution trend, therefore the time evolution of the correlations for 200-h window are presented in Fig. 7. All East–West components of diurnal harmonics show high correlation values with semidiurnal variance during the first half of the experiment. The high correlations with the bottom drag are most likely due to the dominant effect of increasing semidiurnal variance associated with the spring tide, rather than the increase of the bottom drag (hence the label "Variance", Fig. 7). This is also supported by the very high correlation with the variance maintained by the frequency bands corresponding to the 3rd and 4th diurnal harmonics (including M_3 and M_4) throughout the entire experiment (Figs. 7a and b).

For the 5th and 6th harmonics, however, the correlations in the second half of the experiment (label "Bottom drag", Figs. 6 and 7) show a significantly different behaviour. The velocity amplitudes of these two harmonics show a positive correlation with bottom drag, indicating similar growth-decay trends, while negatively correlated with the semidiurnal variance (opposite growth-decay trends). While the correlation coefficients are not particularly high (maxima slightly above 0.5, Figs. 7c and d), the opposite trends suggest that, during this period, bottom friction dominates the evolution of these harmonics.

4. Discussion

Observations of waves and tidal currents in 3-m depth, near the Ponce de Leon Inlet were used to investigate the importance of wave-induced bottom drag as a mechanism for overtide generation. The effect is difficult to observe in general, as it tends to be masked by the stronger effect of tidal current amplitude, and should exhibit a distinct trend for an unambiguous detection. Identifying processes related to wave-induced bottom drag is complicated by the fact that drag-induced modulation is intrinsically weaker than the modulation by tide/overtide variance, and that its effects depend critically on the structure of the wave field (wave period, energy and direction).

Despite the limited scope of the data used (e.g., duration of deployment, spatial coverage, etc.), the analysis suggests that if wave

Author's personal copy

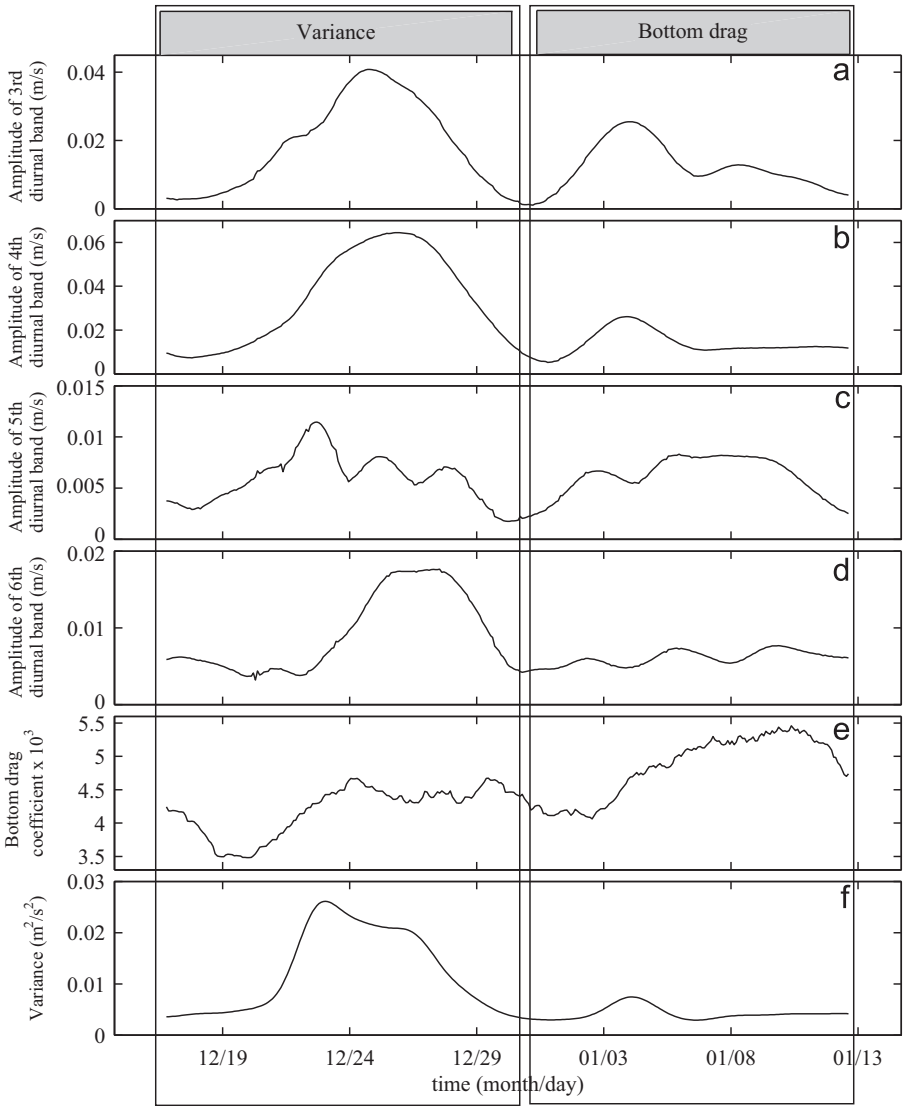

Fig. 6. Evolution of overtide amplitude (East–West component of velocity) of: (a) 3rd, (b) 4th, (c) 5th, and (d) 6th diurnal harmonics, compared with (e) running average of wave-induced bottom drag coefficient; and (f) evolution of the variance at the semidiurnal frequency band.

activity is energetic enough (in this experiment, effective wave-fields had periods >4 s and heights >15 cm) it can cause a consistent increase (70% on average herein) in the bottom drag experienced by currents (Fig. 3). Results derived from applying a windowing analysis process (windowed correlation and Fourier transform) suggest that wave-induced drag can enhance nonlinear effects that generate tidal harmonics at frequencies higher than semidiurnal frequency.

Different harmonics seem to be affected to different degrees by bottom drag variability. In this particular experiment, observations were unambiguous only for the East–West component of the velocity for two of the four harmonics analyzed. The reason for this selective effect is not clear. One may speculate that in this experiment, because the main flow is along North–South axis, the modulation due to the variability of semidiurnal amplitudes dominates the North–South component of overtides but is less effective in modulating the East–West component. In contrast, wave-induced bottom drag has a weak directional variability, increasing only by approximately 2% if waves are assumed to propagate in the direction of the current. Due to scale separation effects (e.g., decay of variance with frequency, resulting in weaker interaction between widely different frequencies), higher harmonics should be less influenced by diurnal–semidiurnal variability, and more by wave-enhanced drag effects.

The observations presented here suggest the hypothesis that wave-generated bed processes (bed ripples) induce bottom-drag variability that could be significant enough to result in nonlinear overtide generation. The limits of the data set (e.g., measurement of currents at a single point in the water column) have forced the results to be based mostly on the bottom drag calculations of a boundary layer model which accounts for wave–current interaction. Using a more sophisticated combined wave-tide model or a 3-D circulation model in order to reproduce the observations would be useful to evaluate the findings, however, such an approach is a major modeling effort and would have its own uncertainties here (e.g., unknown boundary conditions due to limits of the data set). The lateral inertia and curvature effects at the measurement point could possibly enhance the nonlinearities and overtide generation especially during spring tides, however, these effects would probably not be related to conditions that result in a bottom drag increase, and therefore not mask bottom drag effects. A more systematic investigation of surface gravity waves as an overtide generating mechanism likely requires high temporal and spatial resolution observations of wave dynamics,

Author's personal copy

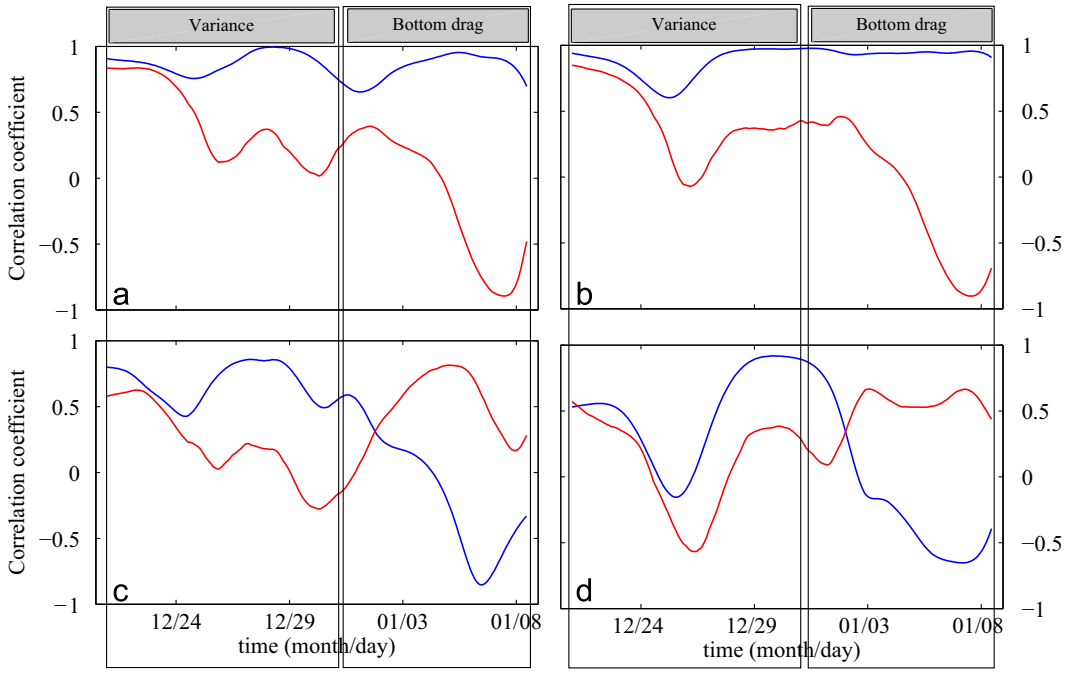

Fig. 7. Coefficient of correlation between diurnal harmonics (amplitude of the East–West component of flow velocity), and: bottom drag coefficient (continuous line); semidiurnal variance (dashed line). The coefficients are calculated for (a) 3rd, (b) 4th, (c) 5th , and (d) 6th diurnal harmonic band (see also Fig. 6).

bottom velocity structure, and associated bedforms, collected over a longer interval which may allow a comparison between similar tidal conditions but different wave conditions. Such an analysis is necessary to support the suggestive results obtained herein and motivate further related studies.

Acknowledgments

We would like to thank to three anonymous reviewers for their constructive suggestions which improved the original manuscript.

References

Bricker, J.D., Inagaki, S., Monismith, S.G., 2005. Bed drag coefficient variability under wind waves in a tidal estuary. J. Hydraul. Eng. 131, 497–508.
Bricker, J.D., Monismith, S.G., 2007. Spectral wave-turbulence decomposition. J. Atmos. Ocean. Technol. 24, 1479–1487.
Carmona, R., Hwang, W.-L., Torresani, B., 1998. Practical Time-Frequency Analysis: Gabor and Wavelet Transforms with an Implementation in S. Academic Press.
Dean, R.G., Dalrymple, R.A., 1991. Water Wave Mechanics for Engineers and Scientists, reprinted Singapore. World-Scientific Publishing Co.
Dworak, J.A., Gomez-Valdes, J., 2005. Modulation of shallow water tides in an inlet-basin system with a mixed tidal regime. J. Geophys. Res. 110, C01007, doi:10.1029/2003JC001865.
Fredsoe, J., Deigaard, R., 1992. Mechanics of Coastal Sediment Transport. Advanced Series on Ocean Engineering, vol. 3. World Scientific, 369pp.
Friedrichs, C.T., Aubrey, D.G., 1994. Tidal propagation in strongly convergent channels. J. Geophys. Res. 99 (C2), 3321–3336.
Grant, W.D., Madsen, O.S., 1979. Combined wave and current interaction with a rough bottom. J. Geophys. Res. 84 (C4), 1797–1808.
Grant, W.D., Madsen, O.S., 1986. The continental-shelf bottom boundary layer. Annu. Rev. Fluid Mech. 18, 265–305.
Hughes, S.A., 1999. Coastal Engineering Technical Note CETN IV-18 U.S. Army Engineer and Development Center, Vicksburg, MS 〈http://chl.erdc.usace.army.mil/library/publications/chetn/pdf/cetn-iv-18.pdf〉.
Jenkins, G.M., Watts, D.G., 1968. Spectral Analysis and its Applications. Emerson-Adams, Boca Raton, Florida 525pp.
Kirby, J.T., Chen, T.-M., 1989. Surface waves on vertically sheared flows: approximate dispersion relations. J. Geophys. Res. 94 (C1), 1013–1027.
Lohrmann, A., Hackett, B., Roed, L.P., 1990. High resolution measurements of turbulence, velocity and stress using a pulse-to-pulse coherent sonar. J. Atmos. Ocean. Technol. 7, 19–37.
Lueck, R.G., Lu, Y., 1997. The logarithmic layer in a tidal channel. Cont. Shelf Res. 17, 1785–1801.
Nielsen, P., 1992. Coastal Bottom Boundary Layers and Sediment Transport. Advanced Series on Ocean Engineering, vol. 4. World Scientific, 324pp.
Parker, B.B., 1991. The relative importance of the various non-linear mechanisms in a wide range of tidal interactions review. In: Parker, B.B. (Ed.), Tidal Hydrodynamics. John Wiley, Hoboken, NJ, pp. 237–268.
Parker, B.B., 2007. Tidal Analysis and Prediction. NOAA Special Publication NOS CO-OPS 3, Maryland, 378pp.
Pawlowicz, R., Beardsley, B., Lentz, S., 2002. Classical tidal harmonic analysis including error estimates in MATLAB using T-TIDE. Comput. Geosci. 28, 929–937.
Phillips, O.M., 1958. The equilibrium range in the spectrum of wind-generated waves. J. Fluid Mech. 4, 426–434.
Rosman, J.H., Hench, J.L., Koseff, J.R., Monismith, S.G., 2008. Extracting Reynolds stresses from acoustic doppler current profiler measurements in wave-dominated environments. J. Atmos. Ocean. Technol. 25, 286–306.
Shaw, W.J., Trowbridge, J.H., 2001. The direct estimation of near-bottom turbulent fluxes in the presence of energetic wave motions. J. Atmos. Ocean. Technol. 18, 1540–1557.
Signell, R.P., Beardsley, R.C., Graber, H.C., Capotondi, A., 1990. Effect of wave-current interaction on wind-driven circulation in narrow, shallow embayments. J. Geophys. Res. 95 (C6), 9671–9678.
Smith, J.M., 2002. Wave pressure gauge analysis with current. J. Waterway Port Coastal Ocean Eng. 128 (6), 271–275.
Stacey, M.T., Monismith, S.G., Burau, J.R., 1999. Measurements of Reynolds stress profiles in an unstratified tidal flow. J. Geophys. Res. 104 (C5), 10933–10949.
Styles, R., Glenn, S.M., 2000. Modeling stratified wave and current bottom boundary layers on the continental shelf. J. Geophys. Res. 105 (C10), 24119–24139.
Styles, R., Glenn, S.M., 2002. Modeling bottom roughness in the presence of wave-generated ripples. J. Geophys. Res. 107 (C8), 3110, doi:10.1029/2001JC000864.